Improved Chemical and Electrochemical Stability on Perovskite Oxides by Less Reducible Cations at the Surface

Nikolai Tsvetkov[1,2,†], Qiyang Lu[1,3 †], Lixin Sun[1,2], Ethan Crumlin[4], and Bilge Yildiz[1,2,3,]*

[1] Laboratory for Electrochemical Interfaces, [2] Department of Nuclear Science and Engineering, [3] Department of Material Science and Engineering, Massachusetts Institute of Technology, 77 Massachusetts Avenue, Cambridge, Massachusetts 02139, United States.

[4]Advanced Light Source, Lawrence Berkeley National Laboratory, Berkeley, California 94720, United States

[†] These authors contributed equally to this work.

[*] Corresponding author. E-mail: byildiz@mit.edu

Abstract

Segregation and phase separation of aliovalent dopants on perovskite oxide (ABO_3) surfaces is detrimental to the performance of energy conversion systems such as solid oxide fuel/electrolysis cells and catalysts for thermochemical H_2O and CO_2 splitting. One key reason behind the instability of perovskite oxide surfaces is the electrostatic attraction of the negatively charged A-site dopants (for example, Sr'_{La}) by the positively charged oxygen vacancies ($V_O^{\cdot\cdot}$) enriched at the surface. Here we show that reducing the surface $V_O^{\cdot\cdot}$ concentration improves the oxygen surface exchange kinetics and stability significantly, albeit contrary to the well-established understanding that surface oxygen vacancies facilitate reactions with O_2 molecules. We take $La_{0.8}Sr_{0.2}CoO_3$ (LSC) as a model perovskite oxide, and modify its surface with additive cations that are more and less reducible than Co on the B-site of LSC. By using ambient pressure X-ray absorption and photoelectron spectroscopy, we proved that the dominant role of the less reducible cations is to suppress the enrichment and phase separation of Sr while reducing the concentration of $V_O^{\cdot\cdot}$ and making the LSC more oxidized at its surface. Consequently, we found that these less reducible cations significantly improve stability, with up to 30x acceleration of the oxygen exchange kinetics, after 54 hours in air at 550 ^{o}C achieved by Hf addition onto LSC. Finally, the results revealed a "volcano" relation between the oxygen exchange kinetics and the oxygen vacancy formation enthalpy of the binary oxides of the additive cations. This volcano relation highlights the existence of an optimum surface oxygen vacancy concentration that balances the gain in oxygen exchange kinetics and the chemical stability loss.

The chemical instability of the perovskite oxide surfaces due to cation segregation and phase precipitation limits the performance and durability in multiple applications, including solid oxide fuel and electrolysis cells (SOFC/SOEC)[1,2], thermochemical[3] and photo-assisted[4] water splitting. State-of-the-art SOFC cathode materials, exemplified by $La_{0.6}Sr_{0.4}CoO_3$[5], $La_{0.6}Sr_{0.4}Co_{0.2}Fe_{0.8}O_3$ (LSCF)[6], and $Ba_{0.5}Sr_{0.5}Co_{0.8}Fe_{0.2}O_3$ (BSCF)[7] suffer from degradation of surface chemistry and oxygen reduction reaction (ORR) kinetics at elevated temperatures[8-13]. This degradation is because of Sr segregation and separation of SrO-like insulating phases at the perovskite surface[8,11,14-17], sometimes in the form of complete coverage of the surface by SrO[15], blocking the electron transfer and oxygen exchange pathways[18] and leaving a dopant-poor sub-surface region. The consequence is detrimental for electrochemical performance, by up to two orders of magnitude loss in ORR kinetics[9,10]. One proposed way against this challenge has been coating of LSC[19,20] or LSCF[13] surfaces with several nm thick layers of $La_{0.8}Sr_{0.2}MnO_3$[13,20] or ZrO_2[19]. Although some enhancement in electrode stability was shown by these surface coatings, the underlying mechanisms behind the improvement of the cathode stability have not yet been made clear, making it difficult to go beyond these empirical observations.

In our previous work, the electrostatic attraction of negatively charged dopants to the surface that is enriched with positively charged oxygen vacancies was recognized as an important driving force for Sr segregation on perovskite oxides[11]. Consequently, it is reasonable to expect that a lower concentration of oxygen vacancies can improve the surface stability and ORR kinetics. This may appear contradictory to the well-established understanding that oxygen vacancies facilitate ORR[21] and other reactions of small molecules on transition metal oxides[22-24]. However, significant degradation of the ORR kinetics because of dopant segregation and phase separation is also associated with surface oxygen vacancies[11]. Therefore, here we propose to decrease the surface oxygen vacancy concentration for suppressing the electrostatic driver to this detrimental process.

In this paper we hypothesized that the perovskite oxide surface stability can be tuned as a function of the reducibility of the surface. We took $La_{0.8}Sr_{0.2}CoO_3$ as a model system, and systematically modified its surface with additive cations, whose binary oxides have lower (V^{5+})[25] or higher (Nb^{5+}, Ti^{4+}, Zr^{4+}, Hf^{4+}, and Al^{3+})[25-29] enthalpy of oxygen vacancy formation compared to that of LSC[30]. We introduced these additives to the LSC surface at sub-monolayer coverages

by a simple method using metal chloride solutions,[31,32] and we refer to these surface modified samples as LSC-Me (see Supporting Information (SI), Table S1 for details). We found that the less reducible cations, i.e. Hf^{4+}, Ti^{4+}, Zr^{4+}, Nb^{5+} or Al^{3+}, improve the oxygen exchange kinetics and stability on LSC, while the addition of V and excess Co lead to stronger degradation. Ambient-pressure X-ray photoelectron spectroscopy (AP-XPS) and X-ray absorption spectroscopy (AP-XAS)[33,34] measurements up to 550 ^{o}C revealed that these less reducible cations make the LSC surface more oxidized and decrease the surface oxygen vacancy concentration, leading to a smaller electrostatic driving force for Sr segregation.

Electrochemical performance of LSC with surface chemical modifications

We compared the evolution of the surface oxygen exchange coefficients, k^q, which represents the oxygen reduction reactivity of LSC cathodes as a function of time at 530 °C in air. The LSC films treated with chloride solutions of Co, V, Nb, Zr, Ti, Hf, and Al are denoted as LSC-Co12, LSC-V12, LSC-Nb19, LSC-Zr15, LSC-Ti15, LSC-Hf16 and LSC-Al15, respectively. The numbers indicate the Me/(La+Sr+Co+Me) ratio at/near the film surface with Me being the added metal cation at the surface. The k^q obtained from electrochemical impedance spectroscopy are given in Fig. 1a. Initially, all the samples have similar k^q values. Within the first few hours of the measurements, the surface exchange kinetics degraded with varying extents on the different samples. The LSC, LSC-Co12, and LSC-V12 electrodes degraded most severely, with almost 1.5 orders of magnitude decrease of k^q within the 30 hours of testing. The LSC-Ti15, LSC-Zr15, LSC-Hf16, LSC-Nb19 and LSC-Al15 cathodes were more stable, with the best performance by LSC-Hf16 having more than 30 times faster oxygen exchange kinetics than that on LSC after 54 hours.

The morphology of the electrochemically tested cathode surfaces, shown in Fig. 1b, indicates the correlation of the electrochemical stability to the surface chemical stability. On the films with fast degradation of k^q, i.e., LSC and LSC-V12, a large surface roughness and particle coverage is evident. Electrochemically stable films such as LSC-Ti15, LSC-Al15 and LSC-Hf16 have more stable surface morphology with significantly lower roughness. Our previous investigation on the nature of these segregated particles on cobaltites identified them as an insulating SrO-related phase which degrades the surface oxygen exchange[8,14]. From these results,

it is clear that the addition of the less reducible cations prevents the segregation of insulating Sr-rich phases, and improves the electrochemical stability and kinetics significantly (> 10×) compared to pristine LSC.

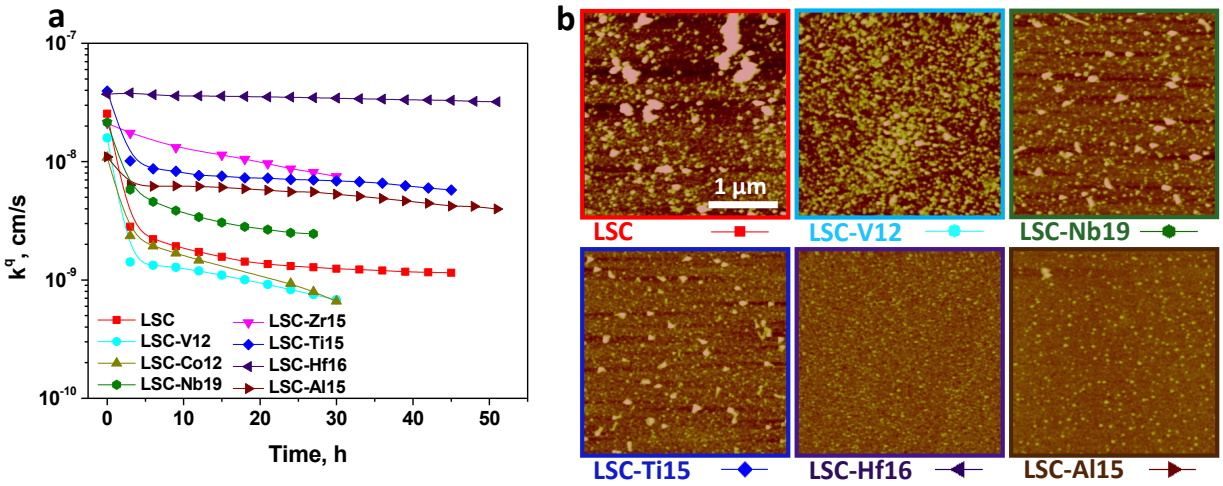

Figure 1. Surface oxygen exchange kinetics and stability on LSC dense thin film cathodes. (a) The oxygen surface exchange coefficient, k^q, quantified from electrochemical impedance spectroscopy measurements over time at 530 °C in air, for the LSC and LSC-Me films. (b) Atomic force microscopy images on the LSC, LSC-V12, LSC-Nb19, LSC-Ti15, LSC-Hf16, and LSC-Al15 films that were electrochemically tested as shown in Fig. 1a.

Evolution of surface chemical composition

APXPS on the pristine LSC and the LSC-Ti3, LSC-Ti15, and LSC-Hf16 films provided more detailed assessment of the surface chemical stability. The experiments were conducted in oxygen pressure (pO_2) from 10^{-6} Torr to 0.76 Torr and up to 550 °C. The analysis of the Sr 3d photoelectron spectra allows to quantify the atomic concentration of Sr at the film surface, and also the Sr binding environments in the perovskite lattice and in a non-lattice phase at the surface ($[Sr]_{Lattice}$ and $[Sr]_{Non\text{-}lattice}$, respectively) (Fig. S5, SI)[8,35]. Our chemical composition analysis showed that the total Sr content and the non-lattice Sr concentration is higher on LSC compared to that on LSC-Ti3, LSC-Ti15, and LSC-Hf16. LSC-Ti15 and LSC-Hf16 have significantly more stable surface Sr composition compared to LSC. $[Sr]_{Total}/([Sr]+[La])$ at the film surfaces is

shown in Fig. 2a. The LSC-Hf16 and LSC-Ti15 films showed only a small increase in the Sr content up to 550 °C. Under the same conditions, $[Sr]_{Total}/([Sr]+[La])$ significantly increased on the bare LSC and on LSC-Ti3. In SI, we demonstrate that the environment temperature and oxygen pressure govern the Sr-chemistry evolution shown in Figure 2, and not temporal variations at each condition (Fig. S6).

The large amount of $[Sr]_{Non\text{-}lattice}$ on the LSC and LSC-Ti3 films (Fig. 2b) are in good agreement with the large coverage of their surface with the segregated particles detected from *ex situ* AFM (Fig. 2d). Thus, the $[Sr]_{Non\text{-}lattice}$ signal can be reasonably attributed to the signal from SrO-rich phase-separated areas of the films[8,14]. The LSC-Hf16 and LSC-Ti15 samples have a significantly smaller amount of $[Sr]_{Non\text{-}lattice}$ (Fig. 2b), a much more stable surface chemistry, with relatively very small amount of phase-separated particles at the surface (Fig. 2d).

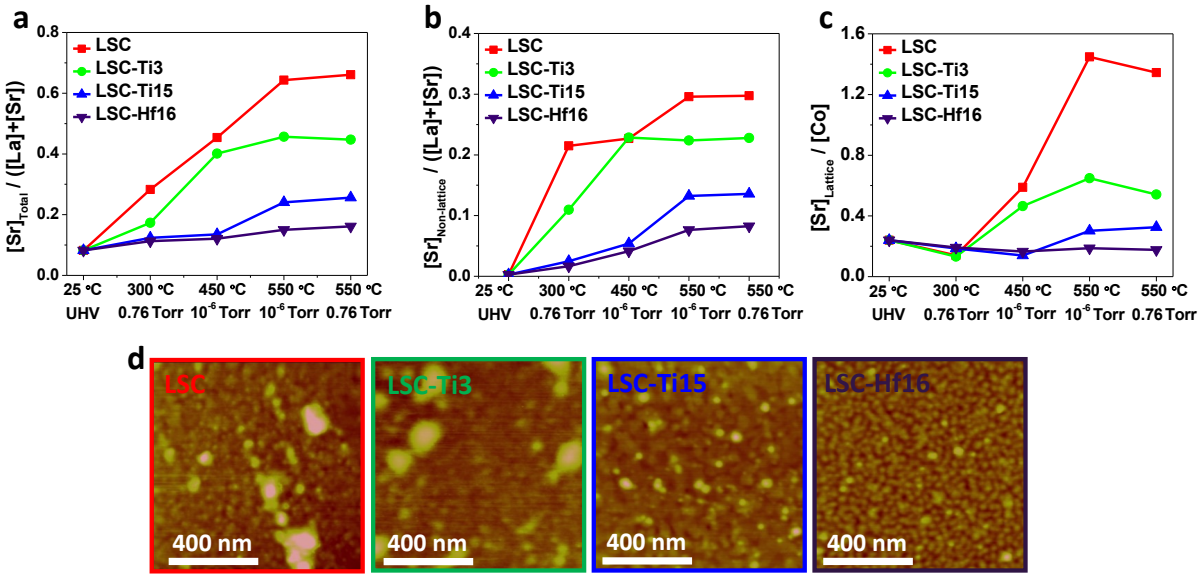

Figure 2. Surface chemical stability on LSC dense thin films. (a) $[Sr]_{Total}/([La]+[Sr])$, (b) $[Sr]_{Non\text{-}lattice}/([La]+[Sr])$, and (c) $[Sr]_{lattice}/[Co]$ ratios at the surface of the LSC and LSC-Me thin films measured *in situ* at different temperature and oxygen partial pressures by ambient pressure X-ray photoelectron spectroscopy (APXPS). (d) *Ex situ* atomic force microscopy images of the LSC and LSC-Me films after the APXPS measurements in (a).

Electronic structure and vacancy concentration on LSC-Me surfaces relative to LSC

In order to reveal the mechanism for improved LSC surface stability with the less reducible cations, we measured the X-ray absorption spectra near the Co $L_{2,3}$ and O K-edges and the valence band (VB) structure, from 10^{-6} Torr to 0.76 Torr of pO_2 and up to 550 ^{o}C. The Co $L_{2,3}$-edge spectra recorded at different conditions for the LSC-Hf16 film are given in Fig. 3a as an example. Chemical shifts of the Co L_3-edge main peak were used for estimating the change in the Co oxidation state. Fig. 3b summarizes the Co L_3-edge position on for LSC, LSC-Ti3, LSC-Ti15, and LSCF-Hf16 measured at 300 °C, 0.76 Torr. The x-axis in Figure 3b, from left to right, points towards an expected lowering of the oxygen vacancy formation enthalpy, or equivalently an expected increase of the oxygen vacancy concentration (based on the effects of Hf and of Ti at different amounts). The variations of the Co L_3-edge positions on these four samples at different conditions are provided in Fig. S7, SI. An increase by +1 in the Co valence, for instance, from Co^{3+} to Co^{4+}, shifts the L_3-edge position by about 1 eV towards higher photon energies[36]. Comparing the peak positions of Co L_3-edge in Fig. 3b, a clear difference in Co valence state among these samples can be seen. At 300 °C, 0.76 Torr, the Co oxidation state increases from LSC to LSC-Ti3, LSC-Ti15, and LSC-Hf16 (Fig. 4b). The shift in L_3-edge position by about +0.4 eV should correspond to an increase of the Co oxidation state by about +0.4 on LSC-Hf16 compared to that on LSC[36]. This trend, at a first glance, is contrary to the fact that Ti^{4+} and Hf^{4+} are electron donors, assuming that these cations occupy the Co^{3+} positions in the perovskite structure. Therefore, the large difference between the L_3-edge positions of the unmodified LSC and the LSC-Hf16 can only be rationalized by a difference in the oxygen vacancy concentration. That is, Hf at the surface decreases the oxygen vacancy concentration, leading to an effectively higher oxidation state of Co. This resulting trend matches qualitatively what we expect based on the oxygen vacancy formation enthalpies in HfO_2, TiO_2, and LSC, also shown in Fig. 3b. Increasing Co oxidation state (i.e. decreasing surface oxygen vacancy concentration) matches the trend of increasing enthalpy of oxygen vacancy formation, ΔH_f^V, such that $\Delta H_f^V(HfO_2) > \Delta H_f^V(TiO_2) > \Delta H_f^V(LSC)$). Note in Fig. 3b that the dashed arrows do not imply a quantitative linearity, but are only a guide to the eye to show the qualitative relation between the Co oxidation state and the reducibility of the binary oxide of the cation added to the surface.

We have excluded the possibility that the different oxidation states from LSC to LSC-Hf16 are caused by different levels of Sr doping, as discussed based on AP-XPS results (SI,

Section 5). It is worth to note that we have limited the comparison of the Co L_3-edge among the samples to the condition at 300 °C, 0.76 Torr, prior to significant Sr segregation on LSC and LSC-Ti3 (SI, Section 5). The AP-XAS results were also supported by measuring the Co 2p core level spectrum by laboratory X-ray source in ultra-high vacuum at ~10^{-9} Torr. We have found Co to be more difficult to reduce on the LSC modified by Nb, Ti, Zr, Hf, and Al, and easier to reduce on the LSC modified by V (Fig. S8, SI).

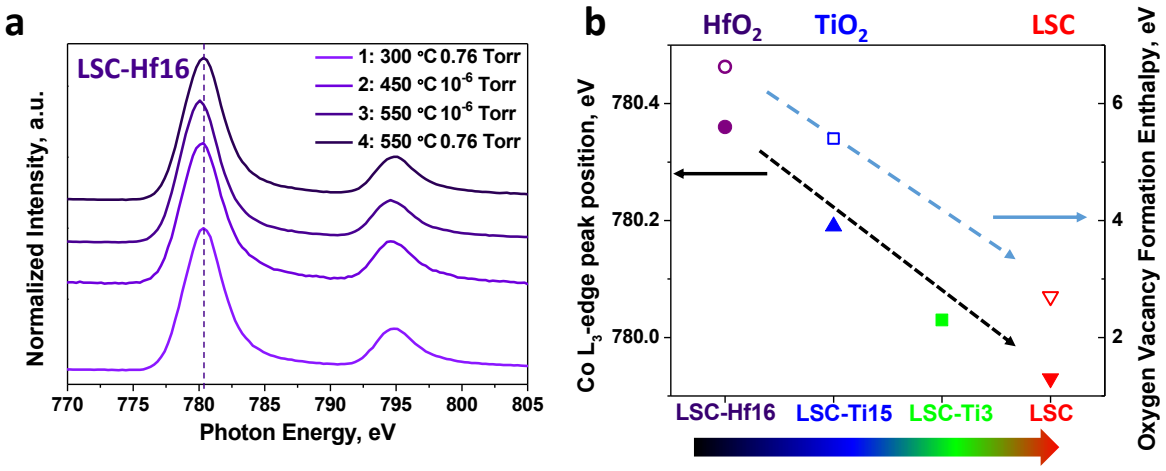

Figure 3. Oxidation state of Co based on Co $L_{2,3}$-edge XAS on LSC dense thin films. (a) Co $L_{2,3}$-edge X-ray absorption spectra on LSC-Hf16 at different temperatures and oxygen partial pressures. The line marks the Co L_3-edge main peak at 300 °C and 0.76 Torr as a reference, to monitor the relative changes in Co oxidation state. (b) The Co L_3-edge peak positions at 300 °C, 0.76 Torr for LSC, LSC-Ti3, LSC-Ti15, and LSC-Hf16 are shown by the solid symbols. The arrow under the x-axis shows the direction of decreasing Co oxidation state, i.e. increasing oxygen vacancy concentration. The open symbols represent the oxygen vacancy formation enthalpy for binary oxides HfO_2[29], TiO_2[26] and also LSC[30]. The dashed arrows in (b) are a guide to the eye and do not imply a quantitative linearity.

We next show that the evolution of the valence band (VB) as well as the O K-edge spectra also support a more oxidized surface when LSC is modified by Hf and Ti, consistent with the Co $L_{2,3}$-edge XAS above. The VB spectra of LSC and LSC-Hf16 films at different conditions are shown in Fig. 4a,b. For the LSC, the intense peak located at around 1.5 eV at 300 °C arises

from the Co t_{2g} states hybridized with the O 2p states[37]. On the other hand, on LSC-Hf16, this peak was absent at the same condition. The intensity of this peak is tied to the number of electrons at the Co t_{2g} orbital[37], and provides information on the Co oxidation state. Therefore, the absence of this peak on LSC-Hf16 indicates that Co is more oxidized than on LSC, in line with the Co L-edge XAS results.

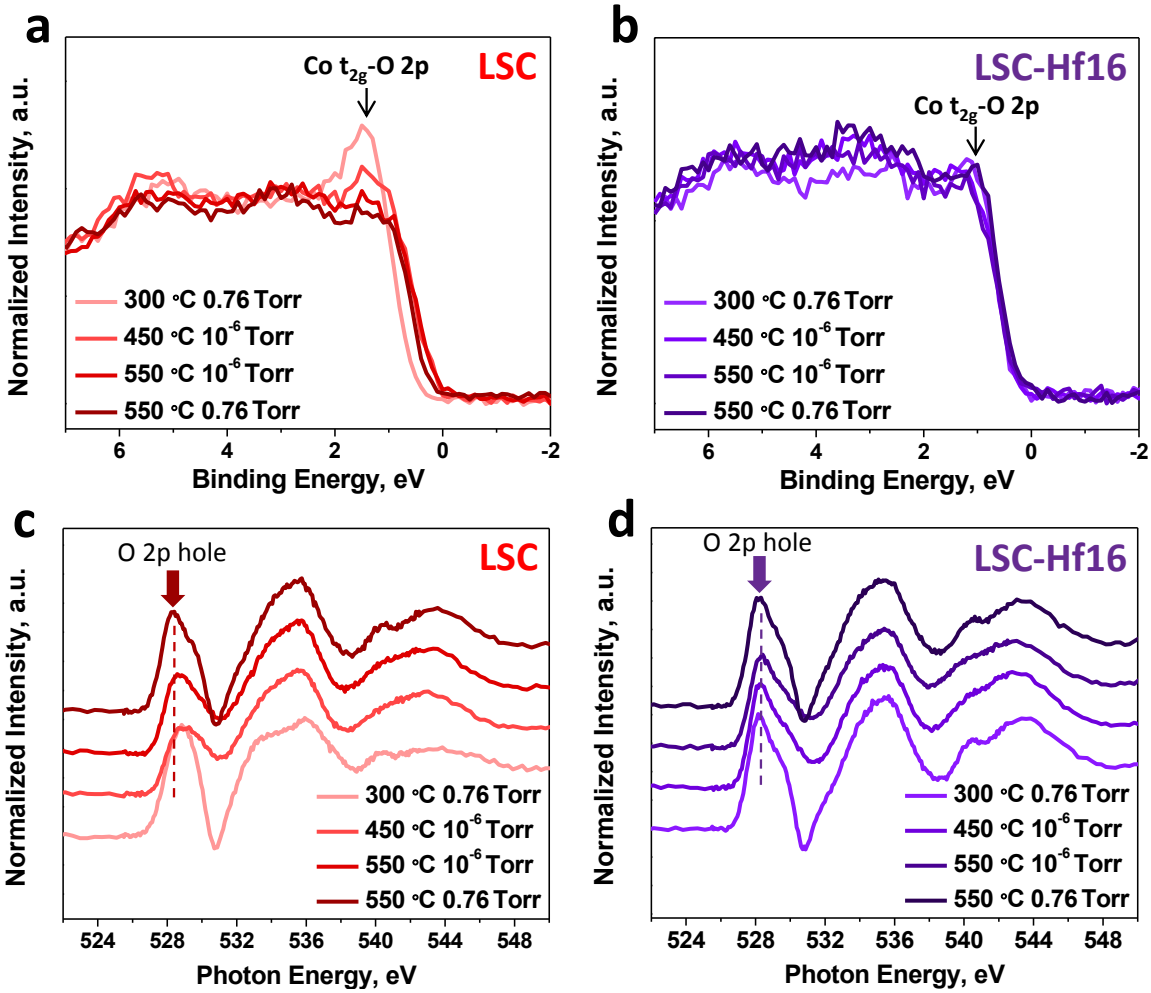

Figure 4. Oxidation state on LSC based on valence band and O K-edge. (a, b) Evolution of the valence band structure from X-ray photoelectron spectra measured *in situ* on (a) LSC and (b) LSC-Hf16. The arrow indicates the low energy peak which reflects the hybridization of Co t_{2g} states with the O 2p orbital. The greater the intensity of this peak, the more electrons in the t_{2g} states of Co. (c, d) O K-edge spectra of (c) LSC and (d) LSC-Hf16 films at different temperatures and oxygen partial pressures. The dashed lines in each plot mark the position of the O 2p ligand hole peak. The presence of this peak indicates p-type doping and therefore an increased Co oxidation state, as seen on LSC-Ti15 and LSC-Hf16.

Figs. 4c,d summarize the evolution of the O K-edge spectra on LSC and LSC-Hf16 films. In line with the unchanged valence band structure (Fig. 4b), the O K-edge spectra on LSC-Hf16 remained unaltered throughout the measurements. A sharp pre-edge peak at around 528 eV (shown by the arrows in Fig. 4d) indicates the existence of O 2p ligand holes on LSC-Hf16[38]. In contrast, this peak was absent on LSC at 300 °C and pO_2 of 0.76 Torr. The presence of this peak indicates increased p-type doping and a more oxidized Co on LSC-Hf16 compared to that on LSC.

The VB and the O K-edge spectra for LSC film surfaces modified by different amounts of Ti are shown in Figs. S9, S10. The evolution of VB and O K-edge on LSC-Ti3 were essentially similar to those of LSC. With a higher concentration of Ti as on LSC-Ti15, the spectra were similar to those of LSC-Hf indicating also a more oxidized Co valence at the surface.

At 450-550 °C, the VB as well as O K-edge XAS of LSC and LSC-Hf16 become similar, with the disappearance of the Co t_{2g} - O 2p peak on LSC, as well as the appearance of the ligand hole pre-edge peak on LSC. The variations of the $[Sr]_{Lattice}$ as a function of temperature can explain this behavior. Raising the temperature up to 450-550 °C substantially increases the $[Sr]_{Lattice}/[Co]$ (Fig. 2c) on LSC and LSC-Ti3. The larger Sr doping level in the near-surface region is charge compensated by Co becoming more oxidized. This decreases the intensity of Co t_{2g}-O 2p peak in the VB and forms the O 2p ligand hole peak in the O K-edge spectra on LSC and LSC-Ti3 at 450-550 °C. As a result, at 300 ^{o}C the difference in the VB and O K-edge among the samples is mainly due to a difference in oxygen vacancy concentrations. On the other hand, at 450-550 °C the enrichment of $[Sr]_{Lattice}$ near the surface of LSC governs the evolution of the VB and the O K-edge spectra.

Bonding environment of the surface additive cations

AP-XAS also allow for extracting the local bonding environment of the cations added onto the LSC surfaces. Fig. 5 shows the Ti $L_{2,3}$-edge on LSC-Ti15 under different measurement conditions. Each $L_{2,3}$-edge shows two peaks due to the crystal field splitting (t_{2g} and e_g states). Comparing the Ti $L_{2,3}$-edge XAS with the spectra reported in literature on TiO_2[39] and $SrTiO_3$[40]

(SI, Fig. S11), we found that the deposited Ti cations on LSC are not coordinated as in TiO_2. Rather, the spectra shape indicates that Ti sits in an octahedral crystal field similar to that of perovskite $SrTiO_3$[40], schematically shown in Fig. 5. This suggests that the Ti cations possibly occupy Co sites in the perovskite lattice of LSC at the surface. By occupying the B-sites in the perovskite, the presence of Ti on LSC can largely change the electronic structure and the oxygen vacancy formation energy of LSC.

Hf, Zr or Nb could not be examined by XAS due to the photon energy of the experiment beamline being limited to 900 eV. Nevertheless, it is known that all of these tested cations can occupy B-sites in perovskite oxides[41-44]. Therefore, we can reasonably assume that similar perovskite-like bonding environments would be obtained also for these transition metal cations (SI, Section 9). Their presence as dopants into the Co-site of LSC alters the oxygen vacancy formation energy at LSC surface because the bonding between the added metal cations and oxygen is much stronger than the Co-O bonds.

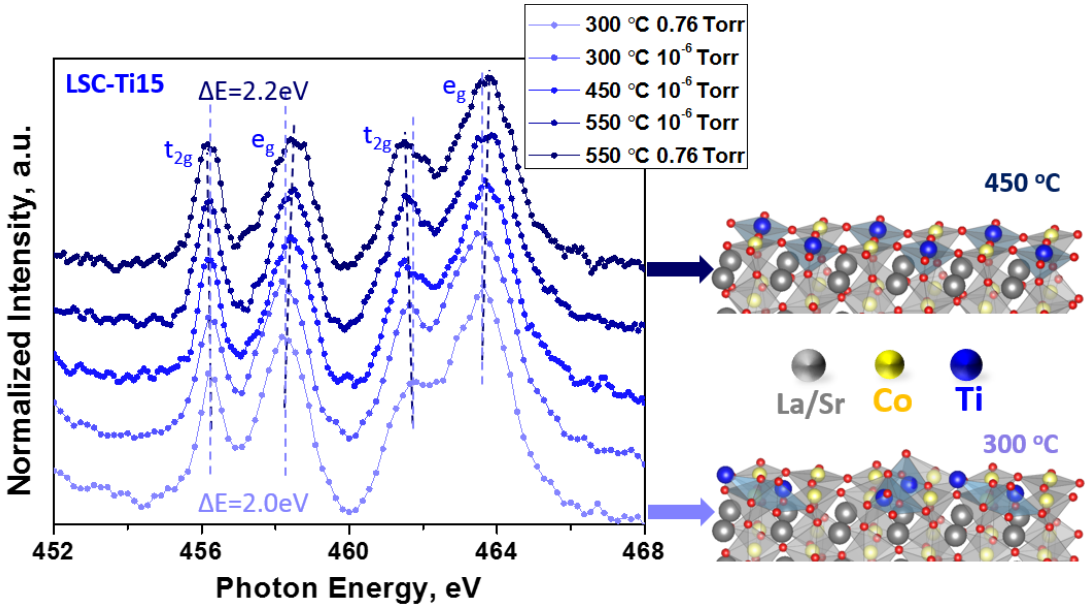

Figure 5. Coordination environment of Ti on LSC-Ti15. Ti $L_{2,3}$-edge X-ray absorption spectra under different measurement conditions. The dashed lines mark the separation of t_{2g} and e_g peaks in both the L_2 and the L_3 edges. Schematic representation of the evolution of the Ti coordination at the LSC surface, from disordered at 300 °C to perovskite coordination of Ti atoms at the B-site of LSC at 450-550 °C (visualized using the VESTA software[45]).

General effect of the surface additive cations on the Sr segregation and ORR kinetics

We can now summarize the effect of the less reducible additive cations on Sr segregation. Upon incorporation into the perovskite lattice at the surface, the less reducible cations, $Me_{Co}^{\cdot}$, can impact the LSC electronic structure and stability in three possible ways: i) $Me_{Co}^{\cdot}$ decreases the surface $V_O^{\cdot\cdot}$ concentration (and lead to a more oxidized Co), and thus, suppress the electrostatic attraction of Sr_{La}' toward the surface, ii) $Me_{Co}^{\cdot}$ provides donor doping and decreases the Co oxidation state, or iii) $Me_{Co}^{\cdot}$ attracts Sr_{La}' toward the surface because of their own positive charge. Based on the obtained *in situ* XPS and XAS data above, we found that ii) and iii) are not evident, while a more oxidized Co is dominant (i.e., outcome i) as shown in Figs. 3,4. This proves that the most likely main effect of the surface doping is to decrease the surface $V_O^{\cdot\cdot}$ concentration (and thus the positive charge) and to relieve the electrostatic attraction of Sr_{La}' toward the surface, thereby suppressing the phase-separation of Sr-rich particles (Figs. 1,2).

It is intriguing to observe that faster and more stable oxygen exchange kinetics was achieved with a decreased oxygen vacancy concentration on LSC. This finding is shown explicitly by the volcano-like dependence of the oxygen exchange kinetic coefficient, k^q, on the difference between the enthalpy of oxygen vacancy formation in the corresponding binary oxide (i.e. MeO_x) and that in LSC (Fig. 6). In this plot, we chose the phases of the binary oxides that are thermodynamically stable under our experimental conditions. Based on this plot, we propose ΔH_f^V of binary oxides MeO_x as a descriptor for the stability of oxygen exchange or ORR kinetics on LSC-Me. As shown in Fig. 6, k^q increases with increasing $\Delta H_f^V(MeO_x)$, reaching peak at LSC-Hf among the tested compositions here. Further increase of $\Delta H_f^V(MeO_x)$ leads to a slower ORR kinetics seen on LSC-Al. We attribute the increase in k^q with increasing $\Delta H_f^V(MeO_x)$ to the decreased surface oxygen vacancy concentration that reduces the electrostatic attraction of Sr and stabilizes the surface cation composition. Further increase of oxygen vacancy formation enthalpy by adding Al onto the surface did not lead to faster ORR kinetics (although it did improve the surface composition stability as shown in Fig. 1b), likely because of a too low

concentration of surface oxygen vacancies as reactive sites. Note the similarity of this plot to the same behavior shown as a function of varying concentration of Ti addition onto LSC (Fig. S13). This volcano plot, to some extent, challenges the well-accepted knowledge that a high oxygen vacancy concentration is desirable in facilitating oxygen exchange kinetics on transition metal oxides[21-25]. It is true that oxygen vacancies do facilitate reactions with oxygen molecules by providing the necessary reaction sites. However, they also drive the detrimental Sr segregation process which slows down the ORR kinetics. We believe that the same concept is applicable not only to LSC but also to other state-of-the-art perovskite oxide catalysts, such as LSCF and BSCF.

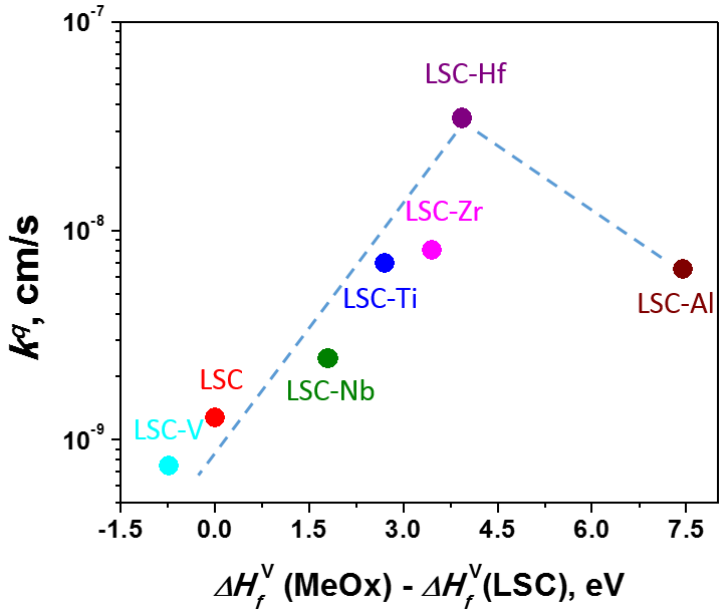

Figure 6. Dependence of oxygen surface exchange kinetics on the reducibility of the LSC surface. The oxygen surface exchange kinetics of LSC-Me, represented by the kinetic coefficient k^q, exhibit a volcano-like dependence on the enthalpy of oxygen vacancy formation (ΔH_f^V) in the binary oxides, MeO_x. The x-axis is the difference between the ΔH_f^V of the binary oxides (i.e. V_2O_5 (α-phase, orthorhombic)[25], Nb_2O_5 (α-phase, orthorhombic)[28], TiO_2 (rutile phase)[25,27], ZrO_2 (monoclinic phase)[29], HfO_2 (monoclinic phase)[29], and Al_2O_3 (α-phase, hexagonal)[26]) and that of LSC[30]. The y-axis shows the oxygen exchange coefficient, k^q, on LSC-Me, where the surface Me concentrations are within 12-19%, measured after 27 hours of testing at 550°C in air. The dashed line is a guide for the eye only.

Conclusion

We achieved significantly improved surface chemical and electrochemical stability on a model perovskite electrocatalyst, LSC, by modifying its surface with less reducible cations. The best performance was achieved by Hf modification of the surface, giving rise to 30x faster oxygen exchange kinetics than that on the unmodified LSC after 54 hours at 530 °C. The dominant effect of introducing these cations on the surface chemistry of LSC was two-fold: i) they reduce the Sr enrichment and phase separation into insulating particles at the surface, and ii) they induce an effectively more oxidized surface with a lower concentration of oxygen vacancies. Both of these outcomes were consistently shown by the Co $L_{2,3}$ edge, O K edge and the VB structure obtained by AP-XPS/XAS. We believe i) is an outcome of ii) – that is, the decrease in the surface oxygen vacancy concentration and the positive charge consequently decreases the electrostatic driving force for Sr'_{La} segregation towards the surface and phase separation. Ti L-edge spectra showed that the additive cations enter a perovskite-like coordination on LSC. Based on this we propose that the surface additive cations serve as dopants and can largely alter the surface electronic structure and reduction enthalpy on LSC. Lastly, we revealed a volcano relation of the stability of the ORR kinetics to the oxygen vacancy formation energy at the surface. This volcano plot indicates that one can optimize the performance of the perovskite type electrocatalysts by finding an optimum oxygen vacancy concentration that balances the gain in ORR kinetics and the chemical stability loss. The proposed approach provides a feasible and novel way of designing stable *and* highly reactive perovskite oxides for electrochemical applications.

Methods

Film fabrication and additive cation deposition at the surface. Dense $La_{0.8}Sr_{0.2}CoO_3$ films were deposited onto substrates using pulsed laser deposition (PLD) with a KrF excimer laser of 248 nm wavelength. The $La_{0.8}Sr_{0.2}CoO_3$ target was purchased from MTI Corp., USA. The films were deposited at

650 °C under oxygen pressure of 10 mTorr on the single crystalline $Yr_{0.08}Zr_{0.92}O_2$ (YSZ) (100) substrates (MTI Corp., USA) with a 15 nm thick $Gd_{0.2}Ce_{0.8}O_2$ interlayer grown at the same conditions as the LSC films. The LSC film thickness was around 25 nm. After the growth process, the films were cooled down to room temperature in 2 Torr of oxygen.

To remove excess Sr and to modify the surface with the metal cations, the LSC thin films were dipped in to aqueous chloride solutions of the corresponding metals[31,32]. The deposition parameters are summarized in Table S1 (SI). For samples which were not treated with the metal cations, the excess surface Sr-rich phase formed during the PLD process was removed by dipping of the films into a 0.1 M HCl aqueous solution for 10 sec at room temperature[10]. After the chemical treatment the films were washed with water and isopropanol and dried in the air flow at 260 °C for 1 min.

Surface chemical composition and morphology of the modified LSC films. We examined the chemical composition and morphology at the surface of the LSC films and the modified LSC films (LSC-Me) using X-ray photoelectron spectroscopy and atomic force microscopy (AFM). The XPS core level peak shapes and atomic fractions of Co, La, and Sr were similar for the as-prepared LSC and LSC-Me films. The LSC-Me films had also comparable additive cation fraction, defined as Me/(La+Sr+Co+Me) of 12-19% at the surface (See SI section 1). The films treated with chloride solutions of Co, V, Nb, Zr, Ti, Hf, and Al are denoted as LSC-Co12, LSC-V12, LSC-Nb19, LSC-Zr15, LSC-Ti15, LSC-Hf16 and LSC-Al15, respectively, where the numbers indicate the Me/(La+Sr+Co+Me) ratio at/near the film surface. The surface morphology of the LSC-Me films in their as-prepared condition was smooth, identical to that of the dilute HCl-treated LSC (Fig. S1, SI). Thus, we hypothesize that the metal additive is deposited in the form of a thin and smooth wetting layer at room temperature before further annealing.

Characterization. A Veeco/Digital Instrument Nanoscope IV was used to perform tapping mode AFM for characterizing the surface morphology. Ex situ XPS measurements have been performed to estimate the surface cation composition using a Perkin-Elmer PHI-5500 ESCA Spectrometer with monochromated Al Kα (1486.65 eV) X-ray source under a base pressure of 10^{-9} Torr with the emission angle of 20°. At this configuration, the photoelectron inelastic mean free paths (IMPF) for La 3d, Sr 3d, Co 2p, V 2p, Ti 2p, Nb 3d, Zr 2p, and Hf 4d are 0.3 nm, 0.7 nm, 0.3 nm, 0.4 nm, 0.4 nm, 0.6 nm, 0.6 nm, and 0.6 nm, respectively. The quantitative analysis

of the XPS spectra was performed using the Multipack 9.0 software. The XPS experiments at 450-500 °C and at pressure of 10^{-9} Torr were performed to observe the reduction features in the Co 2p peak (with a photoelectron emission angle 90° and an IMFP of ~1 nm), using an Omicron DAR 400 Mg/Al dual anode non-monochromated X-ray source, an Omicron EA 125 hemispherical analyzer and an Al Kα X-ray source.

EIS measurements were performed on asymmetrical cells with the LSC thin film working electrodes grown on YSZ single crystal substrates. Dense platinum current collectors in the form of a grid (25×25 μm^2 of open area in every 50×50 μm^2 repeat unit in the total 7.3×7.3 mm^2 current collector area) were deposited on the LSC thin films by means of photolithography and RF sputtering. Porous Ag layer served as the counter electrode. Platinum wire leads were connected to the current collector and the counter electrode with the aid of the lab-designed mechanical clip made of Pt-Ir 20% alloy wire (4N purity, ESPI metals, Ashland OR). Parstat 2273 potentiostat was used to perform the EIS measurements in the frequency range of 100 kHz to 1 mHz with an AC amplitude of 5 mV and 0 V DC bias at 530 °C in air during up to 54 hours.

The half cells for electrochemical tests had the LSC or LSC-Me thin films as the working electrode and the pasted porous Ag as the counter electrode. The EIS data obtained on the cells (Fig. S4, SI) were modeled with circuits consisting of two R//CPE (a resistor in parallel to a constant phase element) (Fig. S4)[46]. The k^q values were calculated from the surface polarization resistance (arc in the lower frequency region[46,47]) data measured by EIS[48]. The details about the k^q calculations are given in the Section 3 of SI. For selected composition 2-3 samples were tested electrochemically (Fig. S12, SI). Variation of the measured k^q values ranged from +/-10% for bare LSC to +/-40% for LSC-Hf, in part because of the variability in the PLD-prepared base LSC films and, in part, because of the different concentrations of additives that were put at the surface. The results for LSC, LSC-Ti15, and LSC-Hf16 shown in Fig. 2 represent a batch of samples that were deposited at the same time to ensure consistency of the base film. Regardless of the batch of samples, the general trend shown in Fig. 2 reveals the significantly better stability and higher k^q are consistent among all samples with the less reducible additives at the surface. ZView software was used for the data fitting and analysis.

In situ ambient-pressure X-ray photoelectron and absorption spectroscopy (AP-XPS/XAS). Near ambient pressure XPS/XAS measurements at elevated temperatures on surfaces of LSC and LSC-Me thin films were performed at the Beamline 9.3.2, Advanced Light Source, Lawrence Berkeley National Laboratory. The LSC thin films were placed on a ceramic heater, with thermocouples mounted directly onto the surfaces for surface temperature measurement. The XPS/XAS spectra were collected under the following conditions of temperature, T, and oxygen pressure, pO_2: **1**. T = 300 °C, pO_2 = 0.76 Torr; **2**. T = 450 °C, $pO_2 = 1\times10^{-6}$ Torr; **3**. T = 550 °C, $pO_2 = 1\times10^{-6}$ Torr; **4**. T = 550°C, pO_2 = 0.76 Torr. At each condition, samples were equilibrated for 30 min before the measurement, and the XPS and XAS measurements at each condition took about 2-3 hours in total. The XPS spectra were collected at incident photon energy of 370 eV, with the following order: a low-resolution survey with binding energy (BE) of 200eV~-10eV, then high-resolution scans of Sr 3d, La 4d, Co 2p and VB. The IMFP for the photoelectrons was below 0.8 nm for all the spectra collected. For each condition, the XAS spectra of O K-edge and Co $L_{2,3}$-edge were collected right after the XPS measurement. The O K-edge and Co L-edge spectra were collected with photon energy range of 515-580 eV and 760-810 eV, respectively. The XAS spectra were collected using partial electron yield (PEY) mode, with electron kinetic energy of 275 eV and 589 eV for O K-edge and Co L-edge, respectively. This renders IMFPs of emitted electrons to be ~0.7 nm for the O K-edge and ~1.1 nm for the Co L-edge. The normalization of XAS spectra was performed using the ATHENA software[49].

References

1 Neagu, D., Tsekouras, G., Miller, D. N., Ménard, H. & Irvine, J. T. S. In situ growth of nanoparticles through control of non-stoichiometry. *Nat Chem* **5**, 916-923, doi:10.1038/nchem.1773

http://www.nature.com/nchem/journal/v5/n11/abs/nchem.1773.html#supplementary-information (2013).

2 Lee, K. T. & Wachsman, E. D. Role of nanostructures on SOFC performance at reduced temperatures. *MRS Bulletin* **39**, 783-791, doi:doi:10.1557/mrs.2014.193 (2014).

3 Bork, A. H., Kubicek, M., Struzik, M. & Rupp, J. L. M. Perovskite $La_{0.6}Sr_{0.4}Cr_{1-x}Co_xO_{3-\delta}$ solid solutions for solar-thermochemical fuel production: strategies to lower the operation temperature. *Journal of Materials Chemistry A* **3**, 15546-15557, doi:10.1039/c5ta02519b (2015).

4 Hisatomi, T., Kubota, J. & Domen, K. Recent advances in semiconductors for photocatalytic and photoelectrochemical water splitting. *Chemical Society Reviews* **43**, 7520-7535, doi:10.1039/c3cs60378d (2014).

5 Hayd, J., Yokokawa, H. & Ivers-Tiffée, E. Hetero-Interfaces at Nanoscaled (La,Sr)$CoO_{3-\delta}$ Thin-Film Cathodes Enhancing Oxygen Surface-Exchange Properties. *Journal of The Electrochemical Society* **160**, F351-F359, doi:10.1149/2.017304jes (2013).

6 Carter, S. *et al.* Oxygen transport in selected nonstoichiometric perovskite-structure oxides. *Solid State Ionics* **53**, 597-605, doi:http://dx.doi.org/10.1016/0167-2738(92)90435-R (1992).

7 Shao, Z. & Haile, S. M. A high-performance cathode for the next generation of solid-oxide fuel cells. *Nature* **431**, 170-173, doi:http://www.nature.com/nature/journal/v431/n7005/suppinfo/nature02863_S1.html (2004).

8 Cai, Z., Kubicek, M., Fleig, J. & Yildiz, B. Chemical Heterogeneities on $La_{0.6}Sr_{0.4}CoO_{3-\delta}$ Thin Films—Correlations to Cathode Surface Activity and Stability. *Chem. Mater.* **24**, 1116-1127, doi:10.1021/cm203501u (2012).

9 Hjalmarsson, P., Søgaard, M. & Mogensen, M. Electrochemical performance and degradation of $(La_{0.6}Sr_{0.4})_{0.99}CoO_{3-\delta}$ as porous SOFC-cathode. *Solid State Ionics* **179**, 1422-1426, doi:http://dx.doi.org/10.1016/j.ssi.2007.11.010 (2008).

10 Kubicek, M., Limbeck, A., Frömling, T., Hutter, H. & Fleig, J. Relationship between Cation Segregation and the Electrochemical Oxygen Reduction Kinetics of $La_{0.6}Sr_{0.4}CoO_{3-\delta}$ Thin Film Electrodes. *J. Electrochem. Soc.* **158**, B727-B734, doi:10.1149/1.3581114 (2011).

11 Lee, W., Han, J. W., Chen, Y., Cai, Z. & Yildiz, B. Cation Size Mismatch and Charge Interactions Drive Dopant Segregation at the Surfaces of Manganite Perovskites. *Journal of the American Chemical Society* **135**, 7909-7925, doi:10.1021/ja3125349 (2013).

12 Yi, J. & Schroeder, M. High temperature degradation of $Ba_{0.5}Sr_{0.5}Co_{0.8}Fe_{0.2}O_{3-\delta}$ membranes in atmospheres containing concentrated carbon dioxide. *Journal of Membrane Science* **378**, 163-170, doi:http://dx.doi.org/10.1016/j.memsci.2011.04.044 (2011).

13 Zhu, X. *et al.* Development of $La_{0.6}Sr_{0.4}Co_{0.2}Fe_{0.8}O_{3-\delta}$ cathode with an improved stability via $La_{0.8}Sr_{0.2}MnO_{3-\delta}$ film impregnation. *International Journal of Hydrogen Energy* **38**, 5375-5382, doi:http://dx.doi.org/10.1016/j.ijhydene.2013.02.091 (2013).

14 Chen, Y. *et al.* Segregated Chemistry and Structure on (001) and (100) Surfaces of $(La_{1-x}Sr_x)_2CoO_4$ Override the Crystal Anisotropy in Oxygen Exchange Kinetics. *Chemistry of Materials* **27**, 5436-5450, doi:10.1021/acs.chemmater.5b02292 (2015).

15 Druce, J. *et al.* Surface termination and subsurface restructuring of perovskite-based solid oxide electrode materials. *Energy & Environmental Science* **7**, 3593-3599, doi:10.1039/c4ee01497a (2014).

16 Dulli, H., Dowben, P. A., Liou, S. H. & Plummer, E. W. Surface segregation and restructuring of colossal-magnetoresistant manganese perovskites $La_{0.65}Sr_{0.35}MnO_3$. *Phys. Rev. B* **62**, R14629-R14632 (2000).

17 Tellez, H., Druce, J., Kilner, J. A. & Ishihara, T. Relating surface chemistry and oxygen surface exchange in $LnBaCo_2O_{5+\delta}$ air electrodes. *Faraday Discussions*, doi:10.1039/c5fd00027k (2015).

18 Chen, Y. *et al.* Impact of Sr segregation on the electronic structure and oxygen reduction activity of $SrTi_{1-x}Fe_xO_3$ surfaces. *Energy Environ. Sci.* **5**, 7979-7988 (2012).

19 Gong, Y. *et al.* Stabilizing Nanostructured Solid Oxide Fuel Cell Cathode with Atomic Layer Deposition. *Nano Letters* **13**, 4340-4345, doi:10.1021/nl402138w (2013).

20 Lee, D. *et al.* Enhanced Oxygen Surface Exchange Kinetics and Stability on Epitaxial $La_{0.8}Sr_{0.2}CoO_{3-\delta}$ Thin Films by $La_{0.8}Sr_{0.2}MnO_{3-\delta}$ Decoration. *The Journal of Physical Chemistry C* **118**, 14326-14334, doi:10.1021/jp502192m (2014).

21 Kuklja, M. M., Kotomin, E. A., Merkle, R., Mastrikov, Y. A. & Maier, J. Combined theoretical and experimental analysis of processes determining cathode performance in solid oxide fuel cells. *Physical Chemistry Chemical Physics* **15**, 5443-5471, doi:10.1039/c3cp44363a (2013).

22 Bikondoa, O. *et al.* Direct visualization of defect-mediated dissociation of water on TiO_2(110). *Nat Mater* **5**, 189-192 (2006).

23 Diebold, U. The surface science of titanium dioxide. *Surface Science Reports* **48**, 53-229, doi:http://dx.doi.org/10.1016/S0167-5729(02)00100-0 (2003).

24 Schaub, R. *et al.* Oxygen Vacancies as Active Sites for Water Dissociation on Rutile TiO_2. *Physical Review Letters* **87**, 266104 (2001).

25 Ganduglia-Pirovano, M. V., Hofmann, A. & Sauer, J. Oxygen vacancies in transition metal and rare earth oxides: Current state of understanding and remaining challenges. *Surface Science Reports* **62**, 219-270, doi:http://dx.doi.org/10.1016/j.surfrep.2007.03.002 (2007).

26 Carrasco, J., Lopez, N. & Illas, F. First Principles Analysis of the Stability and Diffusion of Oxygen Vacancies in Metal Oxides. *Physical Review Letters* **93**, 225502 (2004).

27 Janotti, A. *et al.* Hybrid functional studies of the oxygen vacancy in TiO_2. *Physical Review B* **81**, 085212 (2010).

28 Kofstad, P. & Anderson, P. B. Gravimetric studies of the defect structure of α-Nb_2O_5. *Journal of Physics and Chemistry of Solids* **21**, 280-286, doi:http://dx.doi.org/10.1016/0022-3697(61)90106-8 (1961).

29 Zheng, J. X., Ceder, G., Maxisch, T., Chim, W. K. & Choi, W. K. First-principles study of native point defects in hafnia and zirconia. *Physical Review B* **75**, 104112 (2007).

30 Mizusaki, J., Mima, Y., Yamauchi, S., Fueki, K. & Tagawa, H. Nonstoichiometry of the perovskite-type oxides $La_{1-x}Sr_xCoO_{3-\delta}$. *Journal of Solid State Chemistry* **80**, 102-111, doi:http://dx.doi.org/10.1016/0022-4596(89)90036-4 (1989).

31 Sommeling, P. M. *et al.* Influence of a TiCl4 Post-Treatment on Nanocrystalline TiO_2 Films in Dye-Sensitized Solar Cells. *The Journal of Physical Chemistry B* **110**, 19191-19197, doi:10.1021/jp061346k (2006).

32 Tsvetkov, N. A., Larina, L. L., Shevaleevskiy, O., Al-Ammar, E. A. & Ahn, B. T. Design of conduction band structure of TiO_2 electrode using Nb doping for highly efficient dye-sensitized solar cells. *Progress in Photovoltaics: Research and Applications* **20**, 904-911, doi:10.1002/pip.2253 (2012).

33 Feng, Z. A., El Gabaly, F., Ye, X., Shen, Z.-X. & Chueh, W. C. Fast vacancy-mediated oxygen ion incorporation across the ceria–gas electrochemical interface. *Nature Communications* **5**, doi:10.1038/ncomms5374 (2014).

34 Grass, M. E. *et al.* New ambient pressure photoemission endstation at Advanced Light Source beamline 9.3.2. *Review of Scientific Instruments* **81**, 053106, doi:doi:http://dx.doi.org/10.1063/1.3427218 (2010).

35 Crumlin, E. J. *et al.* Surface strontium enrichment on highly active perovskites for oxygen electrocatalysis in solid oxide fuel cells. *Energy & Environmental Science* **5**, 6081-6088, doi:10.1039/c2ee03397f (2012).

36 Hu, Z. *et al.* Difference in spin state and covalence between $La_{1-x}Sr_xCoO_3$ and $La_{2-x}Sr_xLi_{0.5}Co_{0.5}O_4$. *Journal of Alloys and Compounds* **343**, 5-13, doi:10.1016/s0925-8388(02)00004-x (2002).

37 Mizokawa, T. *et al.* Photoemission and x-ray-absorption study of misfit-layered (Bi,Pb)-Sr-Co-O compounds: Electronic structure of a hole-doped Co-O triangular lattice. *Physical Review B* **64**, 115104 (2001).

38 Moodenbaugh, a. *et al.* Hole-state density of $La_{1-x}Sr_xCoO_{3-\delta}$ (0~x~0.5) across the insulator/metal phase boundary. *Physical Review B* **61**, 5666-5671, doi:10.1103/PhysRevB.61.5666 (2000).

39 Thomas, A. G. *et al.* Comparison of the electronic structure of anatase and rutile TiO_2 single-crystal surfaces using resonant photoemission and x-ray absorption spectroscopy. *Physical Review B* **75**, 035105 (2007).

40 van der Laan, G. Polaronic satellites in x-ray-absorption spectra. *Physical Review B* **41**, 12366-12368 (1990).

41 Abbate, M. *et al.* Electronic structure and spin-state transition of $LaCoO_3$. *Physical Review B* **47**, 16124-16130 (1993).

42 Copie, O. *et al.* Structural and magnetic properties of Co-doped (La,Sr)TiO_3 epitaxial thin films probed using x-ray magnetic circular dichroism. *Journal of Physics: Condensed Matter* **21**, 406001 (2009).

43 Fabricius, G. *et al.* Electronic structure of cubic $SrHfO_3$: Ferroelectric stability and detailed comparison with $SrTiO_3$. *Physical Review B* **55**, 164-168 (1997).

44 Lee, J. *et al.* Imprint and oxygen deficiency in (Pb,La)$(Zr,Ti)O_3$ thin film capacitors with La-Sr-Co-O electrodes. *Applied Physics Letters* **66**, 1337-1339, doi:doi:http://dx.doi.org/10.1063/1.113234 (1995).

45 Momma, K. & Izumi, F. VESTA 3 for three-dimensional visualization of crystal, volumetric and morphology data. *Journal of Applied Crystallography* **44**, 1272-1276 (2011).

46 Adler, S. B. Factors Governing Oxygen Reduction in Solid Oxide Fuel Cell Cathodes. *Chemical Reviews* **104**, 4791-4844, doi:10.1021/cr020724o (2004).

47 Jamnik, J. & Maier, J. Generalised equivalent circuits for mass and charge transport: chemical capacitance and its implications. *Physical Chemistry Chemical Physics* **3**, 1668-1678, doi:10.1039/b100180i (2001).

48 Baumann, F. S., Fleig, J., Habermeier, H.-U. & Maier, J. Impedance spectroscopic study on well-defined (La,Sr)(Co,Fe)$O_{3-\delta}$ model electrodes. *Solid State Ionics* **177**, 1071-1081, doi:http://dx.doi.org/10.1016/j.ssi.2006.02.045 (2006).

49 Ravel, B. & Newville, M. ATHENA, ARTEMIS, HEPHAESTUS: data analysis for X-ray absorption spectroscopy using IFEFFIT. *Journal of Synchrotron Radiation* **12**, 537-541, doi:doi:10.1107/S0909049505012719 (2005).

Acknowledgments

The authors are grateful for the funding support from the NSF CAREER Award of the National Science Foundation, Division of Materials Research, Ceramics Program, Grant No.1055583, and from NASA and JPL on the Mars Oxygen ISRU Experiment (MOXIE) project. We thank Mostafa Youssef for useful discussions on the defects in LSC and Qiang Liu for experiment assistance at ALS BL 9.3.2. The authors also acknowledge the use of the Center for Materials Science and Engineering, an MRSEC Shared Experimental Facility of NSF at MIT, supported by the National Science Foundation under award number DMR-1419807. The Advanced Light Source is supported by the Director, Office of Science, Office of Basic Energy Sciences, of the U.S. Department of Energy under Contract No. DE-AC02-05CH11231.

Author Contributions: NT and QL prepared the samples. NT performed electrochemical measurements. QL, NT, BY and EC performed XPS and XAS measurements. All authors analyzed and discussed the results and wrote the paper. BY designed and supervised the research.

Additional information

Supplementary Information accompanies this paper.

Competing financial interests

Authors declare no competing financial interests.

Figure captions

Figure 1. Surface oxygen exchange kinetics and stability on LSC dense thin film cathodes. (a) The oxygen surface exchange coefficient, k^q, quantified from electrochemical impedance spectroscopy measurements over time at 530 °C in air, for the LSC and LSC-Me films. (b) Atomic force microscopy images on the LSC, LSC-V12, LSC-Nb19, LSC-Ti15, LSC-Hf16, and LSC-Al15 films that were electrochemically tested as shown in Fig. 1a.

Surface chemical stability on LSC dense thin films. (a) $[Sr]_{Total}/([La]+[Sr])$, (b) $[Sr]_{Non\text{-}lattice}/([La]+[Sr])$, and (c) $[Sr]_{lattice}/[Co]$ ratios at the surface of the LSC and LSC-Me thin films measured *in situ* at different temperature and oxygen partial pressures by ambient pressure X-ray photoelectron spectroscopy (APXPS). (d) *Ex situ* atomic force microscopy images of the LSC and LSC-Me films after the APXPS measurements in (a).

Figure 3. Oxidation state of Co based on Co $L_{2,3}$-edge XAS on LSC dense thin films. (a) Co $L_{2,3}$-edge X-ray absorption spectra on LSC-Hf16 at different temperatures and oxygen partial pressures. The line marks the Co L_3-edge main peak at 300 ^oC and 0.76 Torr as a reference, to monitor the relative changes in Co oxidation state. (b) The Co L_3-edge peak positions at 300 °C, 0.76 Torr for LSC, LSC-Ti3, LSC-Ti15, and LSC-Hf16 are shown by the solid symbols. The arrow under the x-axis shows the direction of decreasing Co oxidation state, i.e. increasing oxygen vacancy concentration. The open symbols represent the oxygen vacancy formation enthalpy for binary oxides HfO_2[29], TiO_2[26] and also LSC[30]. The dashed arrows in (b) are a guide to the eye and do not imply a quantitative linearity.

Figure 4. Oxidation state on LSC based on valence band and O K-edge. (a, b) Evolution of the valence band structure from X-ray photoelectron spectra measured *in situ* on (a) LSC and (b) LSC-Hf16. The arrow indicates the low energy peak which reflects the hybridization of Co t_{2g} states with the O 2p orbital. The greater the intensity of this peak, the more electrons in the t_{2g} states of Co. (c, d) O K-edge spectra of (c) LSC and (d) LSC-Hf16 films at different temperatures and oxygen partial pressures. The dashed lines in each plot mark the position of the O 2p ligand hole peak. The presence of this peak indicates p-type doping and therefore an increased Co oxidation state, as seen on LSC-Ti15 and LSC-Hf16.

Figure 5. Coordination environment of Ti on LSC-Ti15. Ti $L_{2,3}$-edge X-ray absorption spectra under different measurement conditions. The dashed lines mark the separation of t_{2g} and e_g peaks in both the L_2 and the L_3 edges. Schematic representation of the evolution of the Ti coordination at the LSC surface, from disordered at 300 °C to perovskite coordination of Ti atoms at the B-site of LSC at 450-550 °C (visualized using the VESTA software[45]).

Figure 6. Dependence of oxygen surface exchange kinetics on the reducibility of the LSC surface. The oxygen surface exchange kinetics of LSC-Me, represented by the kinetic coefficient k^q, exhibit a volcano-like dependence on the enthalpy of oxygen vacancy formation (ΔH_f^V) in the binary oxides, MeO_x. The x-axis is the difference between the ΔH_f^V of the binary oxides (i.e. V_2O_5 (α-phase, orthorhombic)[25], Nb_2O_5 (α-phase, orthorhombic)[28], TiO_2 (rutile phase)[25,27], ZrO_2 (monoclinic phase)[29], HfO_2 (monoclinic phase)[29], and Al_2O_3 (α-phase, hexagonal)[26]) and that of LSC[30]. The y-axis shows the oxygen exchange coefficient, k^q, on LSC-Me, where the surface Me concentrations are within 12-19%, measured after 27 hours of testing at 550°C in air. The dashed line is a guide for the eye only.